Multi-Electron Visible Light Photoaccumulation on a Dipyridylamine Copper(II)–Polyoxometalate Conjugate Applied to Photocatalytic Generation of CF 3 Radicals

Weixian Wang, Lise-Marie Chamoreau, Guillaume Izzet, Anna Proust, Maylis Orio, Sébastien Blanchard

▶ **To cite this version:**

Weixian Wang, Lise-Marie Chamoreau, Guillaume Izzet, Anna Proust, Maylis Orio, et al.. Multi-Electron Visible Light Photoaccumulation on a Dipyridylamine Copper(II)–Polyoxometalate Conjugate Applied to Photocatalytic Generation of CF 3 Radicals. Journal of the American Chemical Society, 2023, 145 (22), pp.12136-12147. 10.1021/jacs.3c01716 . hal-04165763

HAL Id: hal-04165763

https://hal.sorbonne-universite.fr/hal-04165763v1

Submitted on 19 Jul 2023

HAL is a multi-disciplinary open access archive for the deposit and dissemination of scientific research documents, whether they are published or not. The documents may come from teaching and research institutions in France or abroad, or from public or private research centers.

L'archive ouverte pluridisciplinaire **HAL**, est destinée au dépôt et à la diffusion de documents scientifiques de niveau recherche, publiés ou non, émanant des établissements d'enseignement et de recherche français ou étrangers, des laboratoires publics ou privés.

Multi-electron visible light photoaccumulation on a dipyridylamine copper(II)-polyoxometalate conjugate applied to photocatalytic generation of CF_3 radical.

Weixian Wang,[#] Lise-Marie Chamoreau,[#] Guillaume Izzet,[#] Anna Proust,[#] Maylis Orio*[$] and Sébastien Blanchard*[#]

: Institut Parisien de Chimie Moléculaire, Sorbonne Université, CNRS, F-75005 Paris, France
$: Aix Marseille Université, CNRS, Centrale Marseille, iSm2, UMR CNRS 7313, 13397 Marseille, France

Abstract : Multi-electron visible light photoaccumulation on a dipyridylamine copper(II)-polyoxometalate conjugate applied to photocatalytic generation of CF3 radical.

By Weixian Wang, Lise-Marie Chamoreau, Guillaume Izzet, Anna Proust, Maylis Orio* and Sébastien Blanchard*

This article describes the synthesis and characterization of an organic-inorganic hybrid polyoxometalate functionalized by a short link with a tripodal N based ligand and its copper complex. Upon visible light irradiation, the latter is able to store up to three reducing equivalents. The locus of the reduction is discussed based on physicochemical measurements and DFT calculations. In presence of Togni's reagent, this complex allows for the photocatalytic generation of CF3 radicals, opening the road to valuable synthetic applications.

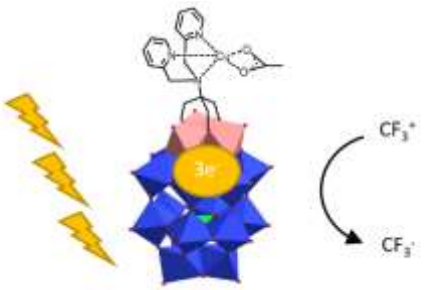

Introduction

Photoredox catalysis is emerging as a major research area for sustainable organic synthesis [1–3] and energy conversion purpose.[4,5] It requires the association of a photoactive antenna to a redox catalyst that is able to accept/release the photogenerated charges to operate the redox reaction. Most reactions in organic chemistry/small molecule activation involve multi-electronic processes, while photosensitizers usually produce monoelectronic charge separation processes. Yet, only a few molecular photoactive systems with a designed charge accumulation site have been described so far.[6–10] The development of an all-integrated system able to absorb visible light energy, accumulate charges to finally use them in a catalytic process is thus of high interest. In this context, polyoxometalates (POMs), i.e. oxo-clusters of early transition metal (Mo, W, V),[11–14] are currently drawing an important attention in the field of photochemistry owing to their photoactivity (often limited to the UV range).[15–17] Among the different POMs, the decatungstate $[W_{10}O_{32}]^{4-}$ polyanion (DT) has retained a considerable interest in photocatalysis owing to its ability to abstract hydrogen atoms upon irradiation.[17–20] POMs have also been associated to molecular chromophores to develop charge photoaccumulation systems[21–23] as they can be reduced with several electrons under minor structural rearrangement.[24,25]

Incorporation of fluorine or fluorinated groups into molecules is widely employed for a variety of applications, ranging from drugs to material science, owing to the highly specific chemical properties of fluorine (e. g. high electronegativity, low Van der Walls radius, low polarizability).[26–30] In particular, a wide range of electrophilic, nucleophilic or even radical trifluoromethyl sources has allowed this field to blossom.[31–34] Among the various proposed methodologies, MacMillan applied in 2019 copper-photoredox dual catalysis to achieve the trifluoromethylation of alkylbromides.[35] The same team then successfully replaced the noble metal iridium photosensitizer by DT, thus developing an original approach relying on more abundant metal ions.[36]

Yet, DT only absorbs in the UV range and can only be functionalized through electrostatic association with a co-catalyst, while numerous POMs can be modified through the covalent anchorage of an organic/organometallic moieties to the POM framework.[37,38] Among these various examples, a few have studied the influence of the POM on the catalytic properties of tethered classical transition metal catalysts. Various advantages of the hybrids, including improved recyclability,[39] electronic delocalization,[30] tunability,[40,41] protection against degradation,[42,43] milder conditions,[44] dual Lewis acid-oxidation catalysis[45] or simply synergy improving yields have been observed.[46] Moreover, some of these hybrid POMs display also appealing photophysical properties.[47–50]

We herein present the synthesis of a copper(II)-polyoxometalate conjugate relying on the grafting of a Cu-dipyridylamine complex onto the surface of the Dawson-type $[P_2V_3W_{15}O_{62}]^{9-}$ polyanion. This all-integrated photosensitizer/charge accumulation/catalyst system is able to store up to three reducing equivalents upon irradiation with visible light. Moreover, its ability to catalytically photogenerate CF_3 radicals, in the presence of a "CF_3^+" source is demonstrated. Finally, this compound shows

improved activity compared to the multi component system, in which the Cu-dipyridylamine complex and the POM are only associated through electrostatic interactions: this outlines the beneficial effect of the covalent anchorage of the Cu-complex onto the POM.

Results and discussion

Synthesis of the POM hybrid ligand

In order to introduce a bioinspired tripodal ligand at close vicinity of the surface of the POM, we first reacted tris(hydroxymethyl)aminomethane with 2-picolylchloride (Figure S1-S3).[51] Subsequent reaction of the obtained 2-[bis(pyridin-2-ylmethyl)amino]-2-(hydroxymethyl)propane-1,3-diol (H_3Tris-DPA) with $(TBA)_5H_4[P_2V_3W_{15}O_{62}]$ (abbreviated D_{V3} hereafter), a mixed polyoxovanadate/polyoxotungstate of the Dawson family, using classical grafting conditions,[52] gave after treatment the hybrid $(TBA)_6$ $[P_2V_3W_{15}O_{59}$(TrisDPA)] (abbreviated **D_{V3DPA}**) in 56% isolated yield (scheme 1).

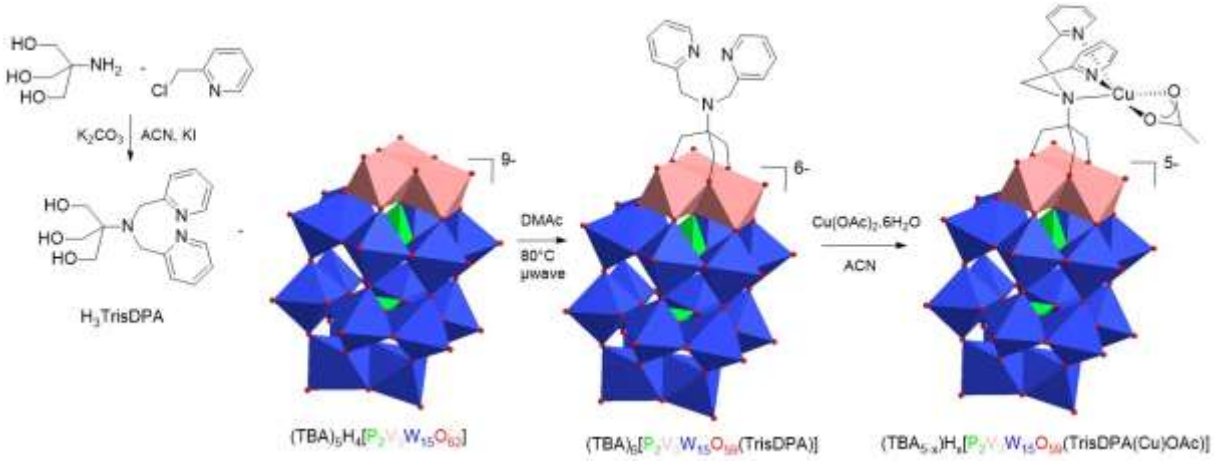

Scheme 1: Synthesis of **D_{V3DPA}{Cu(OAc)}**

D_{V3DPA} has been fully characterized by various techniques. Upon formation of the hybrid, in agreement with Hill's precursor work,[53] the two peaks observed in ^{31}P NMR for the Dawson skeleton are shifted from -7.38 ppm and -12.76 ppm to -6.95 ppm and -13.04 ppm respectively,[46] attesting the grafting of the triester onto the POM surface (Figure S4). The quite small changes, mostly in the relative intensities, of the W-O and V-O stretching region in IR spectroscopy (700-1100 cm^{-1}) confirmed that the Dawson structure was preserved (Figure S5). The isotopic pattern of the adduct $\{TBAH[P_2V_3W_{15}O_{59}(TrisDPA)]\}^{4-}$ at m/z=1114.7948 (z=-4) was detected in HR-MS (Figure S6). Finally, the ^{1}H NMR spectrum, which displayed the characteristic peaks of two equivalent pyridine rings in the aromatic part, together with the expected two types of methylene (NCH_2O and NCH_2Py) and the TBA signature (Figure S7), combined with elemental analysis confirmed the purity of the product. Slow diffusion of diethylether into a concentrated acetonitrile solution afforded crystals suitable for X-ray diffraction studies.

X-ray diffraction studies:

Single crystal X-ray diffraction studies were performed on a plate orange crystal. Crystallographic data are summarized in Table 1.

Table 1 Crystal data and structure refinement for D_{V3DPA}1.5ACN.

Formula	$C_{115}H_{240.5}N_{10.5}O_{62}P_2V_3W_{15}$
Formula weight (g. mol^{-1})	5735.17
Temperature (K)	200
Space group	Pbcn
a/Å	58.129(7)
b/Å	19.830(2)
c/Å	30.818(4)
α/°	90
β/°	90
γ/°	90
Volume/Å^3	35524(7)
Z	8
ρ_{calc}g/cm^3	2.145
μ ($Mo_{K\alpha}$)/mm^{-1}	9.911
Reflections collected	118560
Independent reflections	18566 [R_{int} = 0.0681, R_{sigma} = 0.0482]
Data/restraints/parameters	18566/870/1681
Goodness-of-fit on F^2	1.206
Final R indexes [I>=2σ (I)]	R_1 = 0.0804, wR_2 = 0.1810
Final R indexes [all data]	R_1 = 0.1035, wR_2 = 0.1953
Largest diff. peak/hole / e Å^{-3}	2.11/-2.26
CCDC	2218347

While some important disorder, notably on the TBA cations and one of the pyridine ring, did exist, the X-ray diffraction study clearly showed the successful grafting of the TrisDPA moiety on the POM via V-O-C bond formation. Interestingly, one can measure a fairly short distance of 3.32(3) Å between the tertiary amine of the TrisDPA moiety and the surface of the POM (define as the average plane between the 6 oxygen atoms on top of the vanadium-oxo triad): this should favor a strong electronic communication between the POM skeleton and the grafted complex.

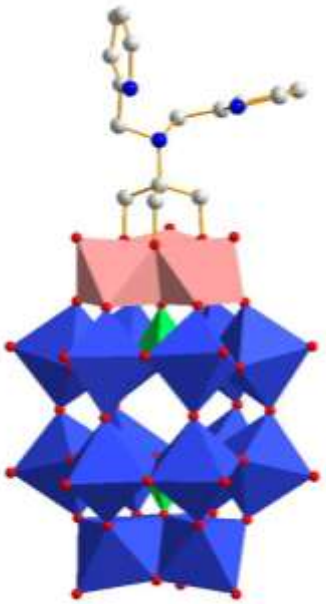

Figure 1: Molecular structure of D_{V3DPA} (TBA cations and hydrogen atoms are omitted for clarity). Blue octahedron: **W**O_6; Pink octahedron: **V**O_6; green tetrahedron: **P**O_4; the trisDPA part is represented with balls and sticks (C in grey; N in blue)

Cu(II)-complexation:

UV-vis titration of a solution of the ligand with copper(II) acetate in acetonitrile showed the appearance of an isosbestic point at 642 nm (Figure 2). Plot of the evolution of the absorbance at 540 nm and 690 nm (inset, Figure 1, black and red respectively) clearly showed a change in the linear adjustment slope after the addition of one equivalent of copper salt in agreement with the formation of a 1:1 complex.

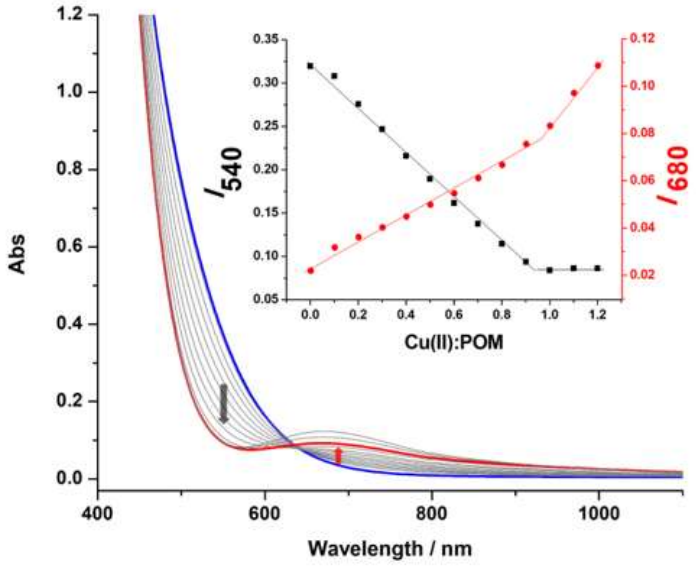

Figure 2: UV-vis titration of $\mathbf{D_{V3DPA}}$ with increasing amount of $Cu^{II}(OAc)_2$. Blue: starting solution; red: upon the addition of one equivalent of Cu(II). Inset: evolution of the absorbance at 540 nm (black) and 680 nm (red) as a function of the number of equivalents of copper ion added.

Precipitation of a 1:1 POM/$Cu(OAc)_2$ mixture in acetonitrile with diethyl ether afforded a green-yellow powder. The resulting product was characterized by ESI-mass spectrometry (Figure S8). The large number of naturally abundant W isotopes, combined with various counter ions, yield to very specific and characteristic, though quite complicated, isotopic patterns.[55,56] Notably, the spectrum displays several signals of anions with z=3 corresponding to the association of the $\{Cu(II)\text{-}D_{V3DPA}\}^{4-}$ with either one H^+ or a TBA cation, and with or without coordinated acetate. For example, the peak at m/z 1427.63 corresponds to $\{H[D_{V3DPA}(Cu^{II})]\}^{3-}$ (calc. m/z = 1427.35) (see SI for further analysis). Elemental analysis in agreement with the formula $(TBA)_{4.8}H_{0.2}[P_2V_3W_{15}O_{59}(TrisDPA(Cu^{II}(OAc)]$ was also obtained, while the IR spectrum showed little variations compared to the free ligand, with essentially two new bands at 1572 cm^{-1} and 1447 cm^{-1}, which correspond to the acetate stretching frequencies (Figure S5).

Upon formation of the complex, only two peaks at -5.94 ppm and -12.62 ppm are present in the ^{31}P NMR spectrum (Figure S9), somewhat shifted compared to the free ligand (-6.95 ppm and -13.04 ppm respectively), confirming the formation of a single new product. The dipicolylamine peaks in ^1H NMR are much more affected, as can be expected from the coordination to a paramagnetic Cu(II) ion. Indeed, as can be seen Figure 3.a and Figure S10, all the aromatic signals and the $N(CH_2Py)_2$ of the free ligand, originally around 8 ppm and 4.3 ppm respectively, completely vanished, and are replaced by broad peaks with paramagnetic chemical shift at 15.30 ppm, 12.81 ppm, 12.23 ppm and -1.14ppm.

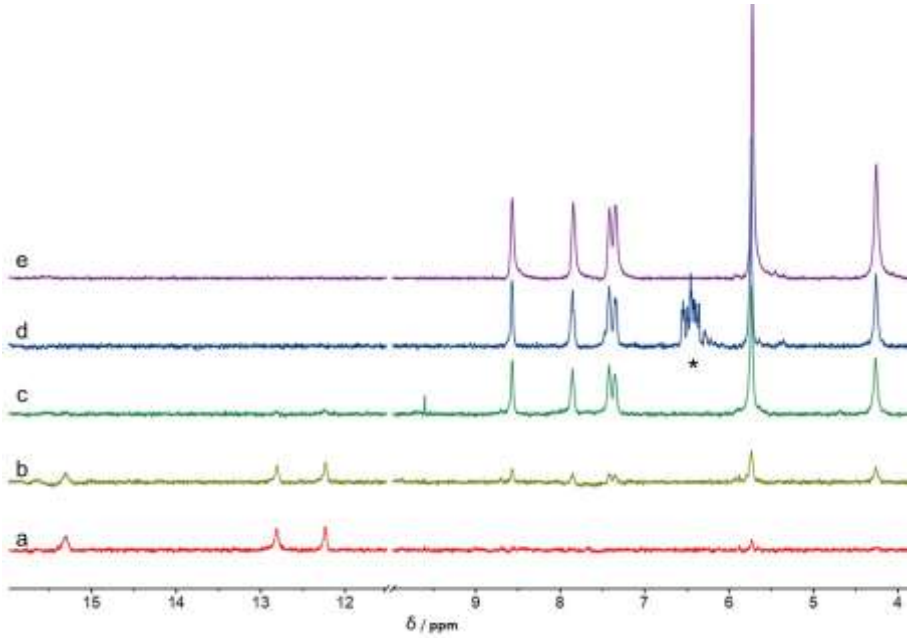

Figure 3: Zoom between 4 ppm and 16 ppm of the ^{1}H NMR spectra in CD_3CN of a) the freshly synthesized complex $(TBA)_{4.8}H_{0.2}[D_{V3DPA}Cu^{II}(OAc)]$ (*red)*, b) after evolution in the NMR tube (*yellow green)*, c) after irradiation (deep green), d) upon reduction with 1eq. $[CoCp_2]$ (*blue)*, e) in situ generated Cu(I) complex (purple). *: ^{1}H NMR signature the of $[Co(Cp)_2]^+$ cation

Cyclic voltammograms of both the ligand and the complex were recorded in acetontitrile, with $TBAPF_6$ as supporting electrolyte.

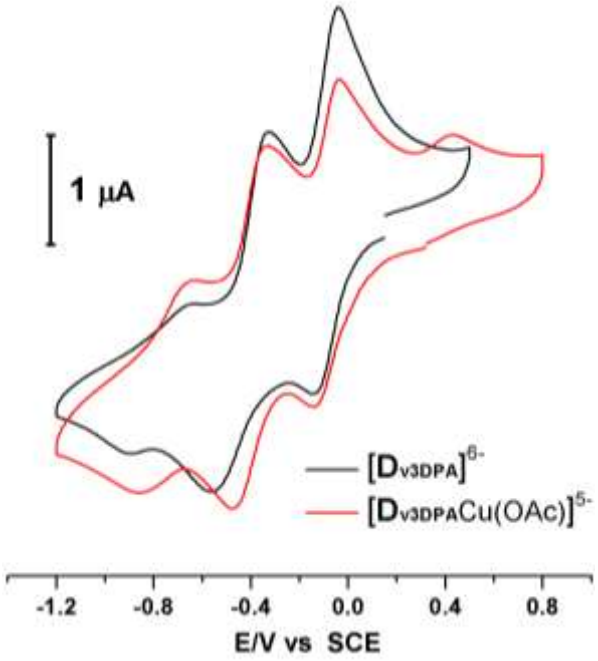

Figure 4: Cyclic voltammograms of 1.0 mmol.L^{-1} solution of D_{V3DPA} (black) and $[D_{V3DPA}Cu^{II}(OAc)]^{5-}$ (red) in CH_3CN (0.1 mol.L^{-1} $TBAPF_6$) at a scan rate of 100 mV s^{-1}.

In the case of the D_{V3DPA} ligand alone, in reduction, two quasi-reversible waves at -0.090 V/SCE and -0.452 V/SCE were observed, followed by a less well-defined process at -0.761 V/SCE (Figure 4, black line). This is in fair agreement with the data for a similar hybrid based on the $[P_2V_3W_{15}O_{62}]^{n-}$ skeleton reported by Ruhlmann and coworker,[57,58] in which three processes are observed at -0.11 V/SCE, -0.48V/SCE and -0.85 V/SCE,[58] and attributed to the successive one electron reduction of the three V^V into V^{IV}. This is also in agreement with the UV-vis signature of these reduced species (vide infra).

Table 2: Electrochemical data in V versus SCE. Half-wave potentials $E_{1/2} = (E_p^{ox} + E_p^{red})/2$. In brackets: $\Delta Ep = E_p^{ox} - E_p^{red}$, in mV.

Product	Cu(II)/Cu(I)			Successive V(V)/V(IV) reduction waves								
				1st			2nd			3rd		
	E_p^{ox}	E_p^{red}	$E_{1/2}$	E_p^{ox}	E_p^{red}	$E_{1/2}$	E_p^{ox}	E_p^{red}	$E_{1/2}$	E_p^{ox}	E_p^{red}	$E_{1/2}$
D_{V3DPA}	-	-	-	-0.044	-0.136	-0.090 (92)	-0.328	-0.576	-0.452 (148)	-0.640	-0.882	-0.761 (242)
D_{V3DPA}{Cu(OAc)}	0.435	*	-	-0.035	-0.145	-0.090 (90)	-0.321	-0.461	-0.391 (140)	-0.634	-0.850	-0.742 (216)

*ill-defined

In the case of the Cu(II) complex, very similar waves were present in the CV when going to negative potentials, and were again attributed to V-centered redox processes (table 2). Moreover, an additional and quite broad redox process appeared at 0.435 V/SCE when going back in oxidation which was attributed to a Cu(I) to Cu(II) reoxidation process. The initial wave associated with the Cu(II) to Cu(I) reduction is very broad and harder to assign, being already started at the resting potential of 0.34 V/SCE (the product has probably already been partially photoreduced from Cu(II) to Cu(I) during the preparation of the experiment, vide infra). Indeed, when a second cycle was recorded in the same CV (Figure S11), a broad reduction wave starts at 0.46V/SCE and is merged with the foot of the first V(V) reduction wave. The lack of electrochemical reversibility of this process is quite common for copper complexes and relates to a change of preferred geometries and ligand affinity between Cu(I) and Cu(II).

These attributions were further confirmed by spectroelectrochemical studies performed on the complex. Upon stepwise reduction of the $[D_{V3DPA}Cu^{II}(OAc)]^{5-}$ at more and more negative potentials, from 0.2 V/SCE down to -1.5 V/SCE, various new signatures were observed (Figure S12). The first reduction process, associated with an electrolysis at about 0V/SCE corresponds to a progressive disappearance of the very weak transition at 690 nm associated with the Cu(II) d-d transition, and the appearance of an isobestic point at 575 nm. This is in agreement with a first process corresponding to a reduction of Cu(II) to Cu(I).

This was followed by a second evolution when setting the potential at -0.4 V/SCE, where a very broad and panchromatic (from 400nm up to 1200nm) absorption did grow, associated with the detection of a second isosbestic point at 455 nm. Upon going to more negative potential (-0.9 V/SCE, behind the third

reduction wave), a new signature arose with changes in the intensity more centered between 600 nm and 900 nm, and these changes were associated with the apparition of another isosbestic point at 423 nm. Finally, a new species was generated when fixing the potential at -1.5 V/SCE, with essentially a growth around 500nm. Regarding these last three successive processes, reduction could either occur at the W or V centers. However, the first W(VI) to W(V) reduction in Dawson POMs is classically associated with a broad absorption growth around 850 nm having ε values of several hundreds to few thousand, while the second W(VI) to W(V) reduction leads to a new band arising around 700 nm, with ε values of a few thousand.[22,49] Thus, the UV-vis signatures of the 2nd, 3rd and 4th reduced species can only be attributed to the successive one electron reductions of the 3 V(V) centers of the POM skeleton into V(IV), and support the attribution proposed for the cyclic voltammetry experiment.

To gain insight into the nature of the species observed by electrochemistry, DFT calculations were undertaken. Considering a DFT-model consisting of $[D_{V3DPA}Cu(OAc)]^{5-}$ surrounded by 5 trimethylammoniun (TMA) cations, the structures of the putative species were subjected to geometry optimization and their electronic properties were investigated. The optimized geometry of $\{(TMA)_5[D_{V3DPA}Cu(OAc)]\}$ showed several close contacts between one TMA and the oxygen atoms of the POM (Figure S13). Electronic structure calculations provided a singly occupied molecular orbital (SOMO, Figure 5a) that is a metal-based orbital while the spin density was found localized at the copper center using Mülliken population analysis (Figure S14a). These data were consistent with the presence of a Cu(II)-POM complex having a doublet (S=1/2) ground spin state. Geometry optimization of the one-electron reduced species $\{(TMA)_5[D_{V3DPA}Cu(OAc)]\}^{-}$ was performed and the resulting structure also displayed close contacts between one TMA and two oxygens from the POM which is likely to have some implications on the electronic structure upon further reduction of the system (Figure S15). The calculated electronic structure supported a metal-based reduction process with the copper center being the reduction locus, leading a Cu(I) complex with a singlet ground spin state (S=0). Looking at the frontier orbitals of $\{(TMA)_5[D_{V3DPA}Cu(OAc)]\}^{-}$ (Figure 5b), we observed that the doubly occupied molecular orbital (DOMO) is metal-based and distributed on the copper center consistent with the formation of the Cu(I) species. Interestingly, the lowest unoccupied orbital (LUMO, Figure 5c) is delocalized on the V centers, which are in close contact to a TMA cation. This implied that the next reduction was likely to occur at the vanadium centers. To further support this assumption, we optimized the doubly-reduced species $\{(TMA)_5[D_{V3DPA}Cu(OAc)]\}^{2-}$ (Figure S16) and analyzed its electronic structure. The geometry of the direduced species still displayed close contacts between the same TMA and oxygens from the POM. Interestingly, the SOMO of this doubly-reduced species is metal based and the spin density is localized mainly at a single vanadium center, the one opposite to the interacting TMA (Figures 5d and S14b). This is in agreement with the 8-line hyperfine pattern observed in EPR for the bi-reduced species, which suggested a localized reduction on one V center only. $\{(TMA)_5[D_{V3DPA}Cu(OAc)]\}^{2-}$ is thus best described as a Cu(I) complex attached to a POM having one

V(IV) center, which is in favor of a POM-based second reduction process presenting a doublet ground spin state (S=1/2). Our DFT findings are thus in good agreement with the experimental observations and help to support the previous assignment of the redox processes.

The computational data were also in line with previous studies in the literature that suggested a net effect of the counterions on the structure, properties and reactivity of POM systems.[59] To further corroborate the influence of the counterion, especially on the electronic structure, we performed additional computations using two extra DFT-models having either 5 Na^+ or (4 Na^+ and 1 TMA^+) counter-ions (Table S1). The models were considered upon one-electron reduction and the relative stability of all possible spin states were calculated. When examining these data, we can observe that the optimized structure of $\{Na_5[D_{V3DPA}Cu(OAc)]\}^-$ (Figure S17) displayed no close contact between the Na and the POM while that of $\{Na_4(TMA)[D_{V3DPA}Cu(OAc)]\}^-$ (Figure S18) featured two interactions between the TMA and the oxygens from the POM. It is worth mentioning that the positioning of the TMA in $\{Na_4(TMA)[D_{V3DPA}Cu(OAc)]\}^-$ is slightly different compared to $\{(TMA)_5[D_{V3DPA}Cu(OAc)]\}^-$ leading to less interactions with the POM oxygens for the former. Such structural features are reflected in the spin state energetics: for both monoreduced $\{Na_5[D_{V3DPA}Cu(OAc)]\}^-$ and $\{Na_4(TMA)[D_{V3DPA}Cu(OAc)]\}^-$ the open-shell singlets resulting from the interaction between a Cu(II) center with a V(IV) center formed upon POM-based first reduction are the most stable spin configurations while for $\{(TMA)_5[D_{V3DPA}Cu(OAc)]\}^-$, we showed that the singlet due to the formation of the Cu(I) species for the first reduction was the ground spin state. Interestingly, the energy separation between the open-shell singlet and the close shell singlet is decreased by 4 $kcal.mol^{-1}$ when including only 1 TMA in the surrounding of the system which highlights the effect of the interactions between the POM and the counterion on the electronic structure. The nature of the counterion that compensates for the negative charge of the Cu-POM complex thus tunes the ground spin state of the system as well as the reduction locus. Moreover, the influence of the counterion on the reduction locus strongly suggest that the first reduction process is very sensitive to the environment, which is in agreement with the electrochemical data and more specifically in line with the overlap of the first reduction wave (Cu-centered) with the second one (V-centered).

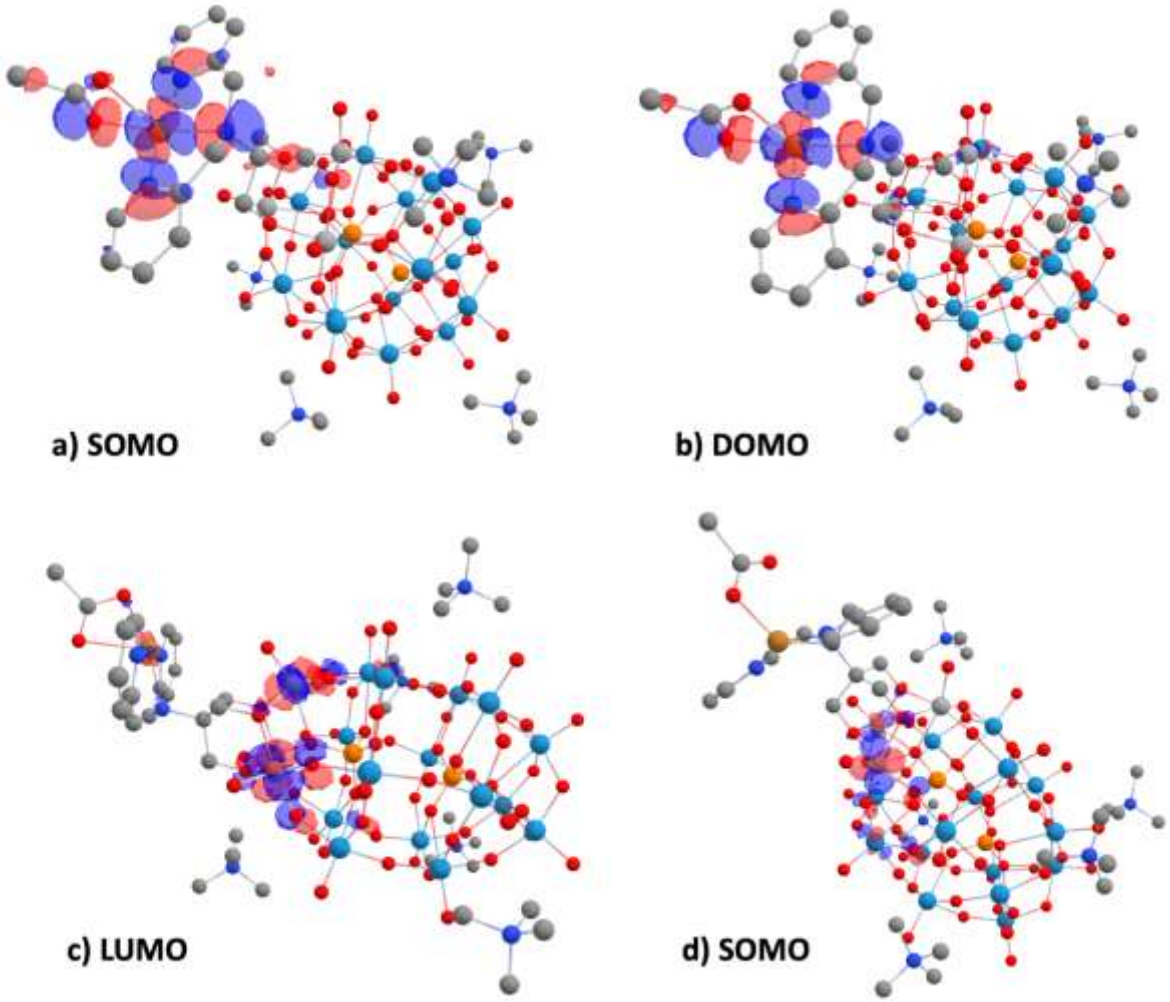

Figure 5: Frontier orbitals: a) SOMO of $\{(TMA)_5[D_{V3DPA}Cu(OAc)]\}$, b) DOMO (HOMO) and c) LUMO of $\{(TMA)_5[D_{V3DPA}Cu(OAc)]\}^{-}$ and d) SOMO of $\{(TMA)_5[D_{V3DPA}Cu(OAc)]\}^{2-}$.

Photoreduction of the complex:

As shown in Figures 3, S19 and S20, an evolution of the NMR signatures is observed with time. While two peaks are observed at -6.89 ppm and -12.99 pm by ^{31}P NMR spectroscopy for a freshly prepared solution of the anion $[D_{V3DPA}Cu(OAc)]^{5-}$ (Figure S19), confirming the presence initially of a single species, the appearance of a new set of signals both in ^{31}P NMR and in the aromatic region (6-9 ppm) of the ^{1}H NMR spectrum of an aged solution indicates an evolution of the solution toward the formation of a diamagnetic species (Figure 3.b). As some POMs (e.g. decatungstate, some Dawson polyoxotungstates or some polyoxovanadates…) are known to possess photoredox properties,[15,60–62] we wondered if these new features could originate from a partial reduction of the copper center due to an electron transfer from a photoreduced POM to the Cu(II) moiety. Indeed, when irradiating the NMR tube with a more powerful light source (with $\lambda > 385$ nm), full conversion of the Cu(II)-complex into a diamagnetic species was observed within 60 minutes (Figure 3.c). Moreover, the addition of one

equivalent of cobaltocene as a chemical reducing agent into a freshly prepared solution of the $[D_{V3DPA}(Cu^{II}(OAc))]^{5-}$ anion resulted in the same ^{1}H NMR (Figure 3.d) and ^{31}P NMR signatures (Figure S19.e), thus confirming the reduction of the complex from paramagnetic Cu(II) to diamagnetic Cu(I). A very similar Cu(I) complex was also generated *in situ* by the addition, under inert atmosphere, of 1 eq. of $[Cu(NCMe)_4]PF_6$ on the D_{V3DPA} ligand in a NMR tube (Figure 3.e).

The addition of a second equivalent of cobaltocene led to the disappearance of the two peaks in ^{31}P NMR, while the ^{1}H NMR showed a slight shift of the peak in the aromatic region, with some line broadening (Figures S19f and S20f) in agreement with a reduction occurring on one of the V^{V} of the polyoxometalate framework.

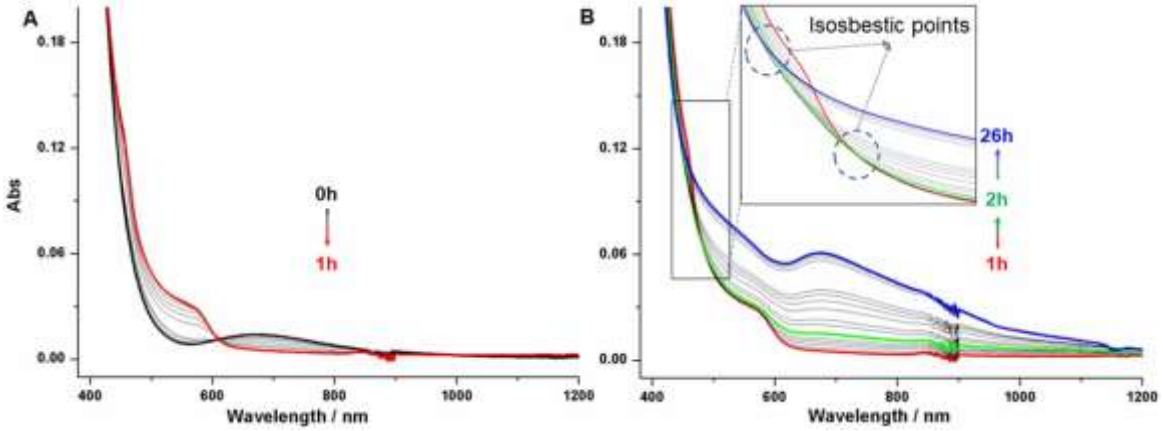

Figure 6: Evolution of the UV-vis signature of a 0.2 mM solution of $[D_{V3DPA}Cu^{II}(OAc)]^{5-}$ in acetonitrile upon visible light irradiation. A. During the first hour of irradiation; B. for the following 26h. Arrows highlight the successive changes of species associated with photoreduction of the complex by 1 (0-1h), 2 (from 1h-2h) or 3 electrons (2h to 26h).

This photoreduction process was followed by UV-vis spectroscopy. Upon visible-light irradiation of the $[D_{V3DPA}Cu^{II}(OAc)]^{5-}$ anion in acetonitrile, a global evolution reminiscent to that of the spectroelectrochemistry experiment was observed. The slight difference in the two evolution profiles probably resulted from different solvation effects of the electrolyte (spectroelectrochemistry) compared to pure acetonitrile (photochemistry). In a first step, the band at 690 nm, assigned to the Cu(II) d-d transition, progressively decreased, in agreement with the reduction of Cu(II) to Cu(I) and the formation of the diamagnetic complex observed by NMR (Figure 6A). In the same time, we observed an increase around 550nm, and a first isosbestic point at 609 nm. Longer irradiation, over about one hour, led to a second process (red to green evolution, Figure 6B) where the absorption at 550 nm remained constant while an overall though modest increase from 600 nm to 1200nm appeared. An isobestic point at 480 nm is associated with this change of species, corresponding to the generation of the 2-electrons reduced form. Finally, upon continuous irradiation up to 2h, conversion to a fourth species, i.e. the 3 electron-reduced species, was observed with the appearance of a new isosbestic point occurring this time at 442nm and associated with a significant increase of the absorption around 700 nm.

This photoreduction was also followed by X-band EPR spectroscopy, freezing the sample in acetonitrile down to 30K. The spectrum of the $[D_{V3DPA}Cu^{II}(OAc)]^{5-}$ anion can be reasonably simulated (Figure S21) with a rhombic g-matrix (g_x=2.240, g_y=2.105, g_z=2.020) with an hyperfine coupling A_x of 490 MHz only detectable on the highest g-value, which is in agreement with a five coordinated Cu(II) ion in an intermediate geometry between bipyramid trigonal and square planar.[63,64] The DFT-computed EPR parameters (g_{max} = 2.231, g_{mid} = 2.077, g_{min} = 2.057) obtained with the optimized structure of $\{(TMA)_5[D_{V3DPA}Cu(OAc)]\}$ agreed well with the experimental values, supporting the presence of an open-shell Cu(II) center leading to a doublet ground spin state for this species (Table S2).
Upon irradiation of the sample, a diminution of the Cu(II) signal was observed, while in the meantime a new pattern appeared, associated with an axial S=1/2, I=7/2 spin system with ($g_{\perp}$=1.97, $A_{\perp}$=180 MHz) and ($g_{//}$= 1.92, $A_{//}$=500MHz), characteristic of the formation of an axial V(IV) species[65,66] (Figure S22). The calculated EPR parameters (g_{max} = 1.983, g_{mid} = 1.982, g_{min} = 1.964) obtained with the optimized structure of $\{(TMA)_5[D_{V3DPA}Cu(OAc)]\}^{2-}$ are consistent with the experimental data, demonstrating that the electronic structure of the direduced species is assigned to doublet ground spin state originating from a Cu(I) center attached to the POM having a V(IV) center carrying the unpaired electron (Table S3).

The combination of the NMR, UV-vis and EPR analyses strengthened by the DFT calculations clearly showed that upon irradiation, $[D_{V3DPA}\{Cu^{II}(OAc)]^{5-}$ was successively photoreduced by up to three electrons, with a first Cu(II) to Cu(I) reduction process followed by two vanadium-centered processes. Although electrochemical storage of numerous electrons is well known in polyoxometalates chemistry,[67] photoaccumulation of two charges has seldom been observed[22,60] and, to the best of our knowledge, three-electron visible light photoreduction of a POM-hybrid has been described only once, very recently, using a POM functionalized with photosensitizers.[23] At this stage, the source of the electron donor has not been identified: adding isopropanol as a sacrificial electron donor allows for the detection on the ^{1}H NMR spectrum of a small amount of acetone, whose integration corresponds only to a small part of the electrons required to reduce the POM with one electron. Other alternative sources, as proposed in the literature, could be the solvent[49] or the TBA cations.[68] A latter possibility could have been oxidation of the -C**H**$_2$O-V linkage of the tethering group as Vanadium(V)-alcoholate are prone to get oxidize into V(IV)-aldehyde. However, the latter is excluded by ^{1}H NMR analysis after catalysis: the spectrum clearly displayed both methylene bridges at 5.7 ppm and 4.3 ppm, with a 3/2 integration between them, and the corresponding pyridine peaks, attesting that the hybrid POM is intact.

Photochemical CF_3-radical generation

Owing to its photoreducing abilities, $[D_{V3DPA}Cu^{II}(OAc)]^{5-}$ is a natural candidate for photocatalytic studies were the copper(I) state could transfer its electron to a valuable substrate. In line with MacMillan's work,[36] reduction of « CF_3^+ » sources like Togni or Umemoto reagents into trifluoromethyl

radical and its catalytic incorporation onto substrate was explored. Visible light irradiation of a mixture of Togni (II) reagent (2eq.) and the $[D_{V3DPA}\{Cu^{II}(OAc)]^{5-}$ anion (1eq.) in the presence of TEMPO radical (2,2,6,6-tetramethylpiperidine-N-oxyl radical) as a CF_3-radical trap led, as monitored by ^{19}F NMR, to the disappearance of the Togni (II) signal at 37.5 ppm and the apparition of a single peak at δ=-55.7 ppm characteristic of the TEMPO-CF_3 adduct (Figure S23),[69] while no reaction occurred in the dark. Following the same reaction by EPR, the starting solution displayed initially the triplet signal of TEMPO at g = 2 as the only observable signature. The latter progressively decreased upon irradiation, following the conversion of TEMPO to TEMPO-CF_3, and was replaced by the signature of the $[D_{V3DPA}\{Cu^{II}(OAc)]^{5-}$ anion (Figure S24). Further irradiation led, as previously observed, to the decrease of the Cu(II) signature and the progressive appearance of the V(IV) signal, indicating that the POM did retain its integrity. The obvious next step was thus to study the catalytic ability of this hybrid POM to photogenerate CF_3-radicals.

Indeed, when using only 5 mol% of POM for the same reaction, evolution of the ^{19}F NMR clearly indicated the full consumption of Togni (II) and TEMPO reagents and their conversion into TEMPO-CF_3 within 8 hours (Figure 7). When the same reaction was performed in the presence of the triester[53] $[P_2V_3W_{15}0_{59}((OCH_2)_3CCH_3)]^{6-}$ D_{V3Me} as a substitute for the hybrid POM, almost no reaction occurred. Furthermore, adding $Cu(OAc)_2$ and DPA to the latter reaction medium only allowed for the formation of *ca.* 15% TEMPO-CF_3 after 8 hours. This last experiment stresses the importance of the covalent link between the POM and the Cu-moiety, that allows for synergy between the photoactive POM skeleton and the copper ion and thus improves efficiency. Indeed, according to the cyclic voltammetry studies, the clear overlap between the Cu(II)/Cu(I) and first V(V)/V(IV) redox processes in the hybrid is in favour of electronic delocalization between the two moieties. Moreover, the counter ion effect observed with DFT calculations clearly suggested that the location of the photoreduction is very sensitive to the environment, and that the resulting electron on the POM can easily be injected in the copper upon CF_3^+ approach. Such a delocalization cannot occur in the multi-molecular approach.

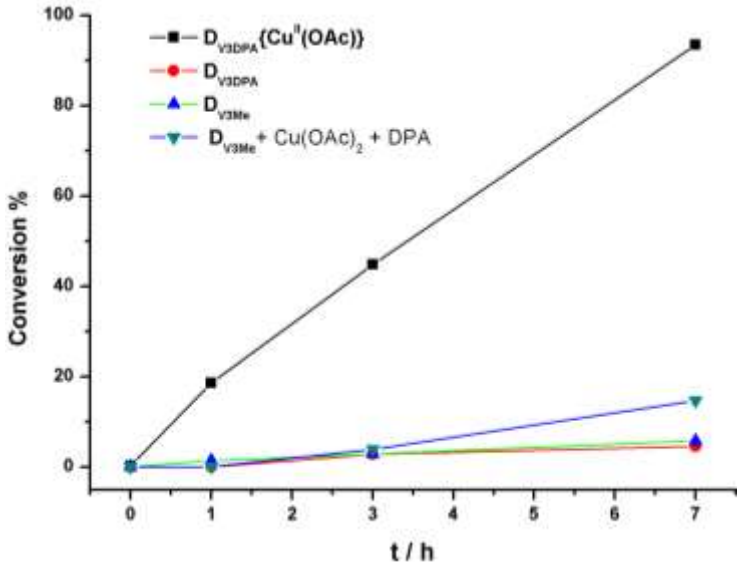

Figure 7 : Evolution of the conversion of Togni reagent ito $TEMPOCF_3$ followed by $^{19}FNMR$ in the presence of **$[D_{V3DPA}\{Cu^{II}(OAc)\}]^{5-}$** anion (black), **$D_{V3DPA}$** (red), **$D_{V3Me}$** (bright green), and **D_{V3Me}** with the mixture of $Cu(OAc)_2$ and DPA (green)

When 20 more equivalent of Togni and TEMPO reactants were added after catalysis, upon irradiation, full conversion to TEMPOCF3 was again observed. This confirmed that the catalyst remains intact after the first cycle.

As no lag time is observed in the catalysis, and since the reduction of "CF_3^+" to CF_3-radical only requires 1 electron, it is likely that as soon as the $[D_{V3DPA}\{Cu^{II}(OAc)]^{5-}$ anion is photo-reduced by 1 electron to generate $H[D_{V3DPA}\{Cu^{I}(OAc)]^{5-}$ the latter reacts with Togni reagent to generate the radical and Ph(I)COOH and the reoxidized Cu(II). The radical is then trapped to TEMPO to give TEMPO-CF_3 and the cycle repeats (scheme 2).

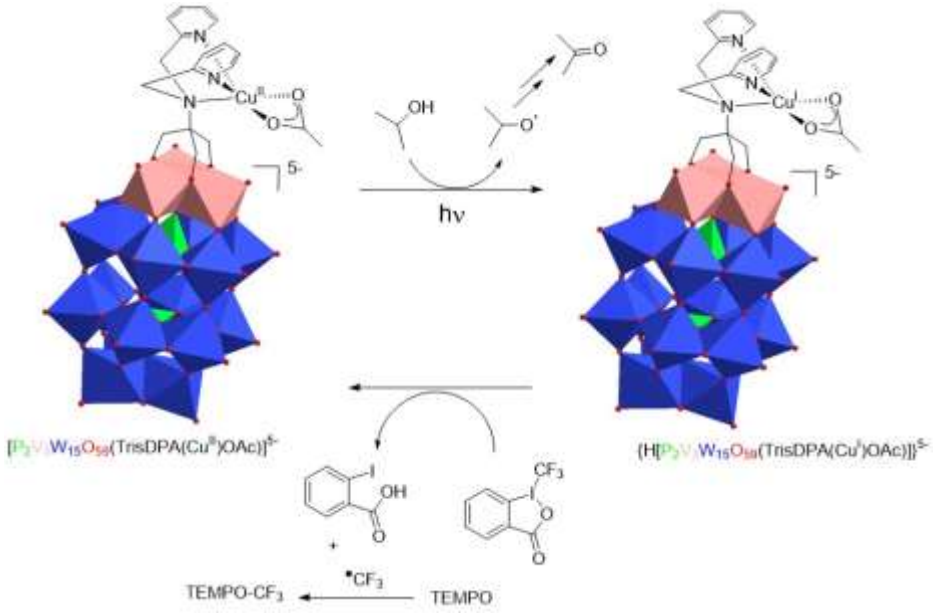

Scheme 2: proposed mechanistic cycle for the trifluoromethylation reaction, using isopropanol as electron source

Conclusion

In this work, we have described the grafting of a Cu(II)-DPA complex on the surface of a mixed V/W Dawson type anion using a modified Tris as a linker bearing a coordination site. This compound has proven to be quite sensitive to light, and is able to store up to 3 electrons upon visible light irradiation. Most notably, although the photoredox properties are associated with the POM skeleton, the first reducing equivalent is stored on the grafted complex. This was confirmed by photophysical studies together with DFT calculations. The latter, however, displayed the major role of the counter-ion in orienting the reduction process, as small ions like Na+, susceptible to come closer to the POM surface, favored a first reduction on the vanadium triad, presumably due to a pronounced electrostatic interaction, whereas calculation with larger alkylammonium led to the experimentally observed Cu- centered redox process. The latter opens the road to Cu-centered reactivity. As a proof of concept, the photoreduced POM was used to catalytically photoreduce Togni's reagent, the generated CF_3 radical being trapped with TEMPO. The presence of a covalent link between the POM skeleton and the complex clearly improves the efficiency of the system compared to the bimolecular approach, and its reactivity toward more valuable substrates is underway. Moreover, owing to the high modularity of the system, where a large array of Nitrogen-based coordination centers, including chiral ligands, could easily be implemented, together with the possible variation on the nature of metal center, this system will be applied to a wide range of applications in the field of photocatalysis, trying to make use of all the electrons stored on the hybrid POM.

Authors information

Corresponding Authors :

Sébastien Blanchard − Institut Parisien de Chimie Moléculaire,

Sorbonne Université, CNRS, F-75005 Paris, France;

Orcid: 0000-0002-5072-5160; Email: sebastien.blanchard@sorbonne-universite.fr

Maylis Orio – Aix Marseille Univ, CNRS, Centrale Marseille, iSm2, Marseille, France

Orcid: 0000-0002-9317-8005; E-mail: maylis.orio@univ-amu.fr

Associated content

Supporting Information

Synthesis protocoles, IR, NMR, UV-Vis, MS and EPR spectra, together with simulation when appropriate, cyclic voltammograms, X-ray diffractions results, and DFT calculations, including energies for frontier molecular orbitals, and Cartesian coordinates are provided in the SI.

Acknowledgment

The Chinese Scholarship Council is acknowledged for the thesis grant of W. Wang. We thank Dr. J.-L. Cantin (INSP, Sorbonne Université, Paris) for graciously providing access to the X-band EPR spectrometer.

EXPERIMENTAL SECTION

Materials and general procedures.

Chemicals and solvents were obtained from Aldrich or Acros. When appropriate, the solvents were dried using solvent purification systems or by distillation under nitrogen from appropriate drying agents and degassed by several freeze−pump−thaw cycles.

1H (400 MHz) and 31P (121.5 MHz) NMR spectra were recorded on a Bruker Avance III Nanobay 400 MHz spectrometer equipped with a BBFO probehead. Chemical shifts are quoted as parts per million (ppm) relative to tetramethylsilane using the solvent signals as a secondary standard for 1H and relative to 85% H3PO4 for 31P (s, singlet; d, doublet; t, triplet; sex, sextet; m, multiplet), and coupling constants (J) are quoted in hertz (Hz). The IR spectrum of the powder was recorded from a KBr pellet on a Jasco FT/IR 4100 spectrometer. Elemental analyses were performed at the Institut des Sciences Analytiques, Villeurbanne, France. High-resolution ESI-MS spectra were recorded using an LTQ Orbitrap hybrid mass spectrometer (Thermofisher Scientific, Bremen, Germany) equipped with an external ESI source operated in the negative-ion mode. Spray conditions typically included a spray voltage of 3 kV, a capillary temperature maintained at 280 °C, a capillary voltage of −30 V, and a tube lens offset of −90 V. Sample solutions in CH3CN (10 pmol.μL−1) were infused into the ESI source by using a syringe pump at a flow rate of 180 μ.h−1. MS spectra were acquired with the Orbitrap analyzer with a theoretical mass resolving power (Rp) of 100000 at m/z 400, after ion accumulation to a target value of 105 and a range detection from m/z 300 to 2000. All data were acquired using external calibration with a mixture of caffeine, a MRFA peptide, and Ultramark 1600 dissolved in Milli-Q water/HPLC-grade CH3CN (50/50, v/v). Cyclic voltammetry was performed in a three-electrode cell, with a glassy carbon working electrode, a platinum counter electrode, and an aqueous saturated calomel electrode (SCE) equipped with a double junction. Spectroelectrochemical studies were conducted in a cell using carbon foam as working electrode and equipped with a Hellma UV−vis immersion probe. UV−visible spectra were recorded at 20°C on a CARY 5000 spectrometer equipped with a Peltier thermostating system. Irradiation was carried out with a 300 W ozone-free Xe lamp (Newport) operated at 280 W and mounted with a water-filled Newport 61945 liquid filter for elimination of IR (λ> 800 nm) irradiation and

Newport 10CGA-385 cut-off filter (λ < 385 nm). The power density measured at 450 nm using a Newport 843-R powermeter coupled to a Newport 818-UV photodiode was 110 µW.cm-2.

X-band EPR spectra were recorded under non-saturating conditions on a Bruker Elexsys 500 spectrometer equipped with an Oxford Instrument continuous-flow liquid helium cryostat and a temperature control system. Simulations of EPR spectra were performed using the Easy Spin Pepper program.70

X-ray diffraction measurements: A single crystal of each compound was selected, mounted onto a cryoloop, and transferred in a cold nitrogen gas stream of an Oxford Cryostream. Intensity data were collected with a BRUKER Kappa-APEXII diffractometer with either graphite-monochromated Mo-Kα radiation (λ = 0.71073 Å) for DV3DPA or microfocused Cu-Kα radiation (λ = 1.54178 Å) for H3TrisDPA. Data collection were performed with APEX2 or 3 suite (BRUKER). Unit-cell parameters refinement, integration and data reduction were carried out with SAINT program (BRUKER). SADABS (BRUKER) was used for scaling and multi-scan absorption corrections.

Crystal structure determination: For DV3DPA, In the Olex2 suite ,71 the structure was solved with SHELXT-14 program and refined by full-matrix least-squares methods using SHELXL-14 . Fourier difference maps were used to locate secondary atoms positions. TBA cations are highly disordered and it was not possible, with this quite low-quality dataset, to locate neither all cations nor all atoms of cations. Geometrical restraints or constraints were applied on distances and a few ones also on angles. Almost all cations are restrained with SIMU/RIGU commands to allow partial anisotropic refinement. A model of disorder was also introduced for pyridine moieties as we were not able to identify one specific position for nitrogen atom. We decided not to introduce geometrical restraints on the hybrid-POM moiety.

For H3TrisDPA :The structure was solved with SHELXT272 and refined anisotropically by full-matrix least-squares methods with SHELXL73 using WinGX.

CCDC 2218347 (DV3DPA) and 2206292(H3TrisDPA) contain the supplementary crystallographic data for this paper. The data can be obtained free of charge from The Cambridge Crystallographic Data Centre via www.ccdc.cam.ac.uk/structures.

DFT calculations:

All calculations were performed using the ORCA program package.74 To facilitate comparisons between theory and experiments, the X-ray crystal structure of DV3DPA was used as a starting point to construct our DV3DPA{Cu(OAc)} models. We have chosen to work with three different models consisting in the DV3DPA{Cu(OAc)} complex surrounded by either 5 Na, 4 Na and one

trimethylammonium (TMA) or 5 TMA cations to evaluate the effect of the counterion nature onto the electronic structure of the resulting complexes. Full geometry optimizations were carried out for all complexes using the GGA functional BP86 75,75,76 by taking advantage of the resolution of the identity (RI) approximation in the Split-RI-J variant 77 with the appropriate Coulomb fitting sets.78 The def2-TZV/P basis set79 was set for the copper complex, while the def2-SVP basis set80 was applied to DV3DPA and its surrounding cations. Increased integration grids (Grid4 in ORCA convention) and tight SCF convergence criteria were used. Dispersion correction was applied according to the method developed by Grimmer with the Becke-Johnson damping scheme (D3BJ).81,82 Electronic structures were obtained from single-point DFT calculations using the hybrid functional B3LYP 83,84 together with the def2-TZVP-(f) basis set. All possible spin configurations were probed from single-point Broken-Symmetry DFT calculations85,86,87 generated with the "FlipSpin" feature of ORCA and using the hybrid functional B3LYP together with the def2-TZVP basis set. For accordance to the experimental conditions, calculations were performed in acetonitrile solvent by invoking the Control of the Conductor-like Polarizable Continuum Model (CPCM).88 EPR parameters, namely g-tensors, for the copper center were obtained from additional single-point calculations using the PBE0 functional.89 The aug-cc-pVTZ-Jmod basis set was applied for the metal center following a protocol recently published by our group.90 Scalar relativistic effects were included using the zeroth-order regular approximation (ZORA) Hamiltonian91,92 with the SARC def2-TZVP(-f) basis sets93,94 and the decontracted def2-TZVP/J Coulomb fitting basis sets for all remaining atoms. For the vanadium centre, g-tensor calculations were performed using the B3LYP functional together with the def2-TZVP basis set. Spin density plots and molecular orbitals were generated using the orca plot utility program and were visualized with the Chemcraft program.

Further information on the synthesis and characterization of all compounds, together with additional reactivity and DFT results are displayed in the supporting information.

References

(1) Crespi, S.; Fagnoni, M. Generation of Alkyl Radicals: From the Tyranny of Tin to the Photon Democracy. *Chem. Rev.* **2020**, *120* (17), 9790–9833. https://doi.org/10.1021/acs.chemrev.0c00278.

(2) Bellotti, P.; Huang, H.-M.; Faber, T.; Glorius, F. Photocatalytic Late-Stage C–H Functionalization. *Chem. Rev.* **2023**, 123 (8), 4237-4352. https://doi.org/10.1021/acs.chemrev.2c00478.

(3) Chan, A. Y.; Perry, I. B.; Bissonnette, N. B.; Buksh, B. F.; Edwards, G. A.; Frye, L. I.; Garry, O. L.; Lavagnino, M. N.; Li, B. X.; Liang, Y.; Mao, E.; Millet, A.; Oakley, J. V.; Reed, N. L.; Sakai, H. A.; Seath, C. P.; MacMillan, D. W. C. Metallaphotoredox: The Merger of Photoredox and Transition Metal Catalysis. *Chem. Rev.* **2022**, *122* (2), 1485–1542. https://doi.org/10.1021/acs.chemrev.1c00383.

(4) Berardi, S.; Drouet, S.; Francàs, L.; Gimbert-Suriñach, C.; Guttentag, M.; Richmond, C.; Stoll, T.; Llobet, A. Molecular Artificial Photosynthesis. *Chem. Soc. Rev.* **2014**, *43* (22), 7501–7519. https://doi.org/10.1039/C3CS60405E.

(5) Zhang, B.; Sun, L. Artificial Photosynthesis: Opportunities and Challenges of Molecular Catalysts. *Chem. Soc. Rev.* **2019**, *48* (7), 2216–2264. https://doi.org/10.1039/C8CS00897C.

(6) Konduri, R.; Ye, H.; MacDonnell, F. M.; Serroni, S.; Campagna, S.; Rajeshwar, K. Ruthenium Photocatalysts Capable of Reversibly Storing up to Four Electrons in a Single Acceptor Ligand: A Step Closer to Artificial Photosynthesis. *Angew. Chem. Int. Ed.* **2002**, *41* (17), 3185–3187. https://doi.org/10.1002/1521-3773(20020902)41:17<3185::AID-ANIE3185>3.0.CO;2-Z.

(7) Pellegrin, Y.; Odobel, F. Molecular Devices Featuring Sequential Photoinduced Charge Separations for the Storage of Multiple Redox Equivalents. *Coord. Chem. Rev.* **2011**, *255* (21–22), 2578–2593. https://doi.org/10.1016/j.ccr.2010.12.017.

(8) Lefebvre, J.-F.; Schindler, J.; Traber, P.; Zhang, Y.; Kupfer, S.; Gräfe, S.; Baussanne, I.; Demeunynck, M.; Mouesca, J.-M.; Gambarelli, S.; Artero, V.; Dietzek, B.; Chavarot-Kerlidou, M. An Artificial Photosynthetic System for Photoaccumulation of Two Electrons on a Fused Dipyridophenazine (Dppz)–Pyridoquinolinone Ligand. *Chem. Sci.* **2018**, *9* (17), 4152–4159. https://doi.org/10.1039/C7SC04348A.

(9) Farran, R.; Le-Quang, L.; Mouesca, J.-M.; Maurel, V.; Jouvenot, D.; Loiseau, F.; Deronzier, A.; Chauvin, J. $[Cr(Ttpy)_2]^{3+}$ as a Multi-Electron Reservoir for Photoinduced Charge Accumulation. *Dalton Trans.* **2019**, *48* (20), 6800–6811. https://doi.org/10.1039/C9DT00848A.

(10) Bürgin, T. H.; Wenger, O. S. Recent Advances and Perspectives in Photodriven Charge Accumulation in Molecular Compounds: A Mini Review. *Energy Fuels* **2021**, *35* (23), 18848–18856. https://doi.org/10.1021/acs.energyfuels.1c02073.

(11) Pope, M. T.; Müller, A. Polyoxometalate Chemistry: An Old Field with New Dimensions in Several Disciplines. *Angew. Chem. Int. Ed. Engl.* **1991**, *30* (1), 34–48. https://doi.org/10.1002/anie.199100341.

(12) Hill, C. L. Introduction: Polyoxometalates Multicomponent Molecular Vehicles To Probe Fundamental Issues and Practical Problems. *Chem. Rev.* **1998**, *98* (1), 1–2. https://doi.org/10.1021/cr960395y.

(13) Hill C. L. Polyoxometalates; Reactivity. In *Comprehensive coordination chemistry II; Polyoxometalates; reactivity*; Ed. D. J. Lockwood, 2004; Vol. 4, pp 635–678.

(14) Long, D.-L.; Burkholder, E.; Cronin, L. Polyoxometalate Clusters, Nanostructures and Materials: From Self Assembly to Designer Materials and Devices. *Chem Soc Rev* **2007**, *36* (1), 105–121. https://doi.org/10.1039/B502666K.

(15) Papaconstantinou, E.; Hiskia, A. Photochemistry and Photocatalysis by Polyoxometalates. In *POLYOXOMETALATED MOLECULAR SCIENCE*; BorrasAlmenar, JJ and Coronado, E and Muller, A and Pope, M, Ed.; NATO SCIENCE SERIES, SERIES II: MATHEMATICS, PHYSICS AND CHEMISTRY; NATO Adv Study Inst; NATO, Sci Affairs Div; Spain Minist Ciencia Tecnol, 2003; Vol. 98, pp 381–416.

(16) Streb, C.; Kastner, K.; Tucher, J. Polyoxometalates in Photocatalysis. *Phys. Sci. Rev.* **2019**, *4* (6), 20170177. https://doi.org/10.1515/psr-2017-0177.

(17) Combs-Walker, L. A.; Hill, C. L. Use of Excited-State and Ground-State Redox Properties of Polyoxometalates for Selective Transfomation of Unactivated Carbon-Hydrogen Centers Remote from the Functional Group in Ketones. *J. Am. Chem. Soc.* **1992**, *114* (3), 938–946. https://doi.org/10.1021/ja00029a022.
(18) Schultz, D. M.; Lévesque, F.; DiRocco, D. A.; Reibarkh, M.; Ji, Y.; Joyce, L. A.; Dropinski, J. F.; Sheng, H.; Sherry, B. D.; Davies, I. W. Oxyfunctionalization of the Remote C−H Bonds of Aliphatic Amines by Decatungstate Photocatalysis. *Angew. Chem. Int. Ed.* **2017**, *56* (48), 15274–15278. https://doi.org/10.1002/anie.201707537.
(19) Ravelli, D.; Fagnoni, M.; Fukuyama, T.; Nishikawa, T.; Ryu, I. Site-Selective C–H Functionalization by Decatungstate Anion Photocatalysis: Synergistic Control by Polar and Steric Effects Expands the Reaction Scope. *ACS Catal.* **2018**, *8* (1), 701–713. https://doi.org/10.1021/acscatal.7b03354.
(20) Capaldo, L.; Ravelli, D.; Fagnoni, M. Direct Photocatalyzed Hydrogen Atom Transfer (HAT) for Aliphatic C–H Bonds Elaboration. *Chem. Rev.* **2021**, 122 (2), 1875-1924. https://doi.org/10.1021/acs.chemrev.1c00263.
(21) Amthor, S.; Knoll, S.; Heiland, M.; Zedler, L.; Li, C.; Nauroozi, D.; Tobaschus, W.; Mengele, A. K.; Anjass, M.; Schubert, U. S.; Dietzek-Ivanšić, B.; Rau, S.; Streb, C. A Photosensitizer–Polyoxometalate Dyad That Enables the Decoupling of Light and Dark Reactions for Delayed on-Demand Solar Hydrogen Production. *Nat. Chem.* **2022**, 1–7. https://doi.org/10.1038/s41557-021-00850-8.
(22) Matt, B.; Fize, J.; Moussa, J.; Amouri, H.; Pereira, A.; Artero, V.; Izzet, G.; Proust, A. Charge Photo-Accumulation and Photocatalytic Hydrogen Evolution under Visible Light at an Iridium(III)-Photosensitized Polyoxotungstate. *Energy Environ. Sci.* **2013**, *6* (5), 1504–1508. https://doi.org/10.1039/C3EE40352A.
(23) Takahashi, M.; Asatani, T.; Morimoto, T.; Kamakura, Y.; Fujii, K.; Yashima, M.; Hosokawa, N.; Tamaki, Y.; Ishitani, O. Supramolecular Multi-Electron Redox Photosensitisers Comprising a Ring-Shaped Re(I) Tetranuclear Complex and a Polyoxometalate. *Chem. Sci.* **2023**, *14* (3), 691–704. https://doi.org/10.1039/D2SC04252E.
(24) Sadakane, M.; Steckhan, E. Electrochemical Properties of Polyoxometalates as Electrocatalysts. *Chem. Rev.* **1998**, *98* (1), 219–238. https://doi.org/10.1021/cr960403a.
(25) Ueda, T. Electrochemistry of Polyoxometalates: From Fundamental Aspects to Applications. *ChemElectroChem* **2018**, *5* (6), 823–838. https://doi.org/10.1002/celc.201701170.
(26) Meanwell, N. A. Fluorine and Fluorinated Motifs in the Design and Application of Bioisosteres for Drug Design. *J. Med. Chem.* **2018**, *61* (14), 5822–5880. https://doi.org/10.1021/acs.jmedchem.7b01788.
(27) General Discussion of Organic Fluorine Chemistry. In *Fluorine in Organic Chemistry*; John Wiley & Sons, Ltd, 2004; pp 1–22. https://doi.org/10.1002/9781444305371.ch1.
(28) Applications of Organofluorine Compounds. In *Modern Fluoroorganic Chemistry*; John Wiley & Sons, Ltd, 2004; pp 203–277. https://doi.org/10.1002/352760393X.ch4.
(29) Berger, R.; Resnati, G.; Metrangolo, P.; Weber, E.; Hulliger, J. Organic Fluorine Compounds: A Great Opportunity for Enhanced Materials Properties. *Chem. Soc. Rev.* **2011**, *40* (7), 3496–3508. https://doi.org/10.1039/C0CS00221F.
(30) Young, N. J.; Pike, V. W.; Taddei, C. Rapid and Efficient Synthesis of [11C]Trifluoromethylarenes from Primary Aromatic Amines and [11C]CuCF3. *ACS Omega* **2020**, *5* (31), 19557–19564. https://doi.org/10.1021/acsomega.0c02027.
(31) Charpentier, J.; Früh, N.; Togni, A. Electrophilic Trifluoromethylation by Use of Hypervalent Iodine Reagents. *Chem. Rev.* **2015**, *115* (2), 650–682. https://doi.org/10.1021/cr500223h.
(32) Liu, X.; Xu, C.; Wang, M.; Liu, Q. Trifluoromethyltrimethylsilane: Nucleophilic Trifluoromethylation and Beyond. *Chem. Rev.* **2015**, *115* (2), 683–730. https://doi.org/10.1021/cr400473a.
(33) Xiao, H.; Zhang, Z.; Fang, Y.; Zhu, L.; Li, C. Radical Trifluoromethylation. *Chem. Soc. Rev.* **2021**, *50* (11), 6308–6319. https://doi.org/10.1039/D1CS00200G.
(34) Alonso, C.; Martínez de Marigorta, E.; Rubiales, G.; Palacios, F. Carbon Trifluoromethylation Reactions of Hydrocarbon Derivatives and Heteroarenes. *Chem. Rev.* **2015**, *115* (4), 1847–1935. https://doi.org/10.1021/cr500368h.

(35) Kornfilt, D. J. P.; MacMillan, D. W. C. Copper-Catalyzed Trifluoromethylation of Alkyl Bromides. *J. Am. Chem. Soc.* **2019**, *141* (17), 6853–6858. https://doi.org/10.1021/jacs.9b03024.
(36) Sarver, P. J.; Bacauanu, V.; Schultz, D. M.; DiRocco, D. A.; Lam, Y.; Sherer, E. C.; MacMillan, D. W. C. The Merger of Decatungstate and Copper Catalysis to Enable Aliphatic C(Sp3)–H Trifluoromethylation. *Nat. Chem.* **2020**, *12* (5), 459–467. https://doi.org/10.1038/s41557-020-0436-1.
(37) Izzet Guillaume; Volatron Florence; Proust Anna. Tailor–Made Covalent Organic-Inorganic Polyoxometalate Hybrids: Versatile Platforms for the Elaboration of Functional Molecular Architectures. *Chem. Rec.* **2016**, *17* (2), 250–266. https://doi.org/10.1002/tcr.201600092.
(38) Anyushin, A. V.; Kondinski, A.; Parac-Vogt, T. N. Hybrid Polyoxometalates as Post-Functionalization Platforms: From Fundamentals to Emerging Applications. *Chem. Soc. Rev.* **2020**, 49,382-432. 10.1039.C8CS00854J. https://doi.org/10.1039/C8CS00854J.
(39) Bar-Nahum, I.; Neumann, R. Synthesis, Characterization and Catalytic Activity of a Wilkinson's Type Metal-Organic–Polyoxometalate Hybrid Compound. *Chem. Commun.* **2003**, 21, 2690–2691. https://doi.org/10.1039/B310236J.
(40) Bar-Nahum, I.; Cohen, H.; Neumann, R. Organometallic−Polyoxometalate Hybrid Compounds: Metallosalen Compounds Modified by Keggin Type Polyoxometalates. *Inorg. Chem.* **2003**, *42* (11), 3677–3684. https://doi.org/10.1021/ic034095s.
(41) Arun, S.; Singh, V. K.; Naz, A.; Narvi, S. S.; Dutta, P. K. A Comparative Catalytic Study Using Different Metal Ions by Incorporating Functionalized Metallosalen into the Lacunary Position of Keggin Polyoxometalate. *J. Indian Chem. Soc.* **2021**, *98* (9), 100118. https://doi.org/10.1016/j.jics.2021.100118.
(42) Berardi, S.; Carraro, M.; Iglesias, M.; Sartorel, A.; Scorrano, G.; Albrecht, M.; Bonchio, M. Polyoxometalate-Based N-Heterocyclic Carbene (NHC) Complexes for Palladium-Mediated C-C Coupling and Chloroaryl Dehalogenation Catalysis. *Chem. – Eur. J.* **2010**, *16* (35), 10662–10666. https://doi.org/10.1002/chem.201001009.
(43) Modugno, G.; Monney, A.; Bonchio, M.; Albrecht, M.; Carraro, M. Transfer Hydrogenation Catalysis by a N-Heterocyclic Carbene Iridium Complex on a Polyoxometalate Platform. *Eur. J. Inorg. Chem.* **2014**, *14*, 2356–2360. https://doi.org/10.1002/ejic.201402020.
(44) Dupré, N.; Brazel, C.; Fensterbank, L.; Malacria, M.; Thorimbert, S.; Hasenknopf, B.; Lacôte, E. Self-Buffering Hybrid Gold-Polyoxometalate Catalysts for the Catalytic Cyclization of Acid-Sensitive Substrates. *Chem. – Eur. J.* **2012**, *18* (41), 12962–12965. https://doi.org/10.1002/chem.201201007.
(45) Riflade, B.; Lachkar, D.; Oble, J.; Li, J.; Thorimbert, S.; Hasenknopf, B.; Lacôte, E. Pd-Containing Organopolyoxometalates Derived from Dawson Polyoxometalate $[P_2W_{15}V_3O_{62}]^{9-}$: Lewis Acidity and Dual Site Catalysis. *Org. Lett.* **2014**, *16* (15), 3860–3863. https://doi.org/10.1021/ol501644c.
(46) Vilona, D.; Lelli, M.; Dumont, E.; Lacôte, E. Organo-Polyoxometalate-Based Hydrogen-Bond Catalysis. *Chem. – Eur. J.* **2021**, *27* (71), 17761–17764. https://doi.org/10.1002/chem.202102807.
(47) Yamase, T. Photo- and Electrochromism of Polyoxometalates and Related Materials. *Chem. Rev.* **1998**, *98* (1), 307–326. https://doi.org/10.1021/cr9604043.
(48) Streb, C. New Trends in Polyoxometalate Photoredox Chemistry: From Photosensitisation to Water Oxidation Catalysis. *Dalton Trans.* **2012**, *41* (6), 1651–1659. https://doi.org/10.1039/C1DT11220A.
(49) Cameron, J. M.; Wales, D. J.; Newton, G. N. Shining a Light on the Photo-Sensitisation of Organic–Inorganic Hybrid Polyoxometalates. *Dalton Trans.* **2018**, *47* (15), 5120–5136. https://doi.org/10.1039/C8DT00400E.
(50) Fujimoto, S.; Cameron, J. M.; Wei, R.-J.; Kastner, K.; Robinson, D.; Sans, V.; Newton, G. N.; Oshio, H. A Simple Approach to the Visible-Light Photoactivation of Molecular Metal Oxides. *Inorg. Chem.* **2017**, *56* (20), 12169–12177. https://doi.org/10.1021/acs.inorgchem.7b01499.
(51) Li, Q.; Peng, Y.; Qian, J.; Yan, T.; Du, L.; Zhao, Q. A Family of Planar Hexanuclear $Co^{III}_4Ln^{III}_2$ Clusters with Lucanidae-like Arrangement and Single-Molecule Magnet Behavior. *Dalton Trans.* **2019**, *48* (34), 12880–12887. https://doi.org/10.1039/C9DT02103E.

(52) Li, J.; Huth, I.; Chamoreau, L.-M.; Hasenknopf, B.; Lacôte, E.; Thorimbert, S.; Malacria, M. Insertion of Amides into a Polyoxometalate. *Angew. Chem. Int. Ed.* **2009**, *48* (11), 2035–2038. https://doi.org/10.1002/anie.200805964.

(53) Hou, Y.; Hill, C. L. Hydrolytically Stable Organic Triester Capped Polyoxometalates with Catalytic Oxygenation Activity of Formula $[RC(CH_2O)_3V_3P_2W_{15}O_{59}]^{6-}$ (R = CH_3, NO_2, CH_2OH). *J. Am. Chem. Soc.* **1993**, *115* (25), 11823–11830. https://doi.org/10.1021/ja00078a022.

(54) Finke, R. G.; Rapko, Brian.; Saxton, R. J.; Domaille, P. J. Trisubstituted Heteropolytungstates as Soluble Metal Oxide Analogs. III. Synthesis, Characterization, Phosphorus-31, Silicon-29, Vanadium-51, and 1- and 2-D Tungsten-183 NMR, Deprotonation, and Proton Mobility Studies of Organic Solvent Solute Forms of $H_xSiW_9V_3O_{40}^{x-7}$ and $H_xP_2W_{15}V_3O_{62}^{x-9}$. *J. Am. Chem. Soc.* **1986**, *108* (11), 2947–2960. https://doi.org/10.1021/ja00271a025.

(55) Wilson, E. F.; Miras, H. N.; Rosnes, M. H.; Cronin, L. Real-Time Observation of the Self-Assembly of Hybrid Polyoxometalates Using Mass Spectrometry. *Angew. Chem. Int. Ed.* **2011**, *50* (16), 3720–3724. https://doi.org/10.1002/anie.201006938.

(56) Debela, A. M.; Ortiz, M.; Beni, V.; Thorimbert, S.; Lesage, D.; Cole, R. B.; O'Sullivan, C. K.; Hasenknopf, B. Biofunctionalization of Polyoxometalates with DNA Primers, Their Use in the Polymerase Chain Reaction (PCR) and Electrochemical Detection of PCR Products. *Chem. - Eur. J.* **2015**, *21* (49), 17721–17727. https://doi.org/10.1002/chem.201502247.

(57) Allain, C.; Schaming, D.; Karakostas, N.; Erard, M.; Gisselbrecht, J.-P.; Sorgues, S.; Lampre, I.; Ruhlmann, L.; Hasenknopf, B. Synthesis, Electrochemical and Photophysical Properties of Covalently Linked Porphyrin–Polyoxometalates. *Dalton Trans.* **2013**, *42* (8), 2745–2754. https://doi.org/10.1039/C2DT31415K.

(58) Azcarate, I.; Ahmed, I.; Farha, R.; Goldmann, M.; Wang, X.; Xu, H.; Hasenknopf, B.; Lacôte, E.; Ruhlmann, L. Synthesis and Characterization of Conjugated Dawson-Type Polyoxometalate–Porphyrin Copolymers. *Dalton Trans.* **2013**, *42* (35), 12688–12698. https://doi.org/10.1039/C3DT50850A.

(59) Toupalas, G.; Karlsson, J.; Black, F. A.; Masip-Sánchez, A.; López, X.; Ben M'Barek, Y.; Blanchard, S.; Proust, A.; Alves, S.; Chabera, P.; Clark, I. P.; Pullerits, T.; Poblet, J. M.; Gibson, E. A.; Izzet, G. Tuning Photoinduced Electron Transfer in POM-Bodipy Hybrids by Controlling the Environment: Experiment and Theory. *Angew. Chem. Int. Ed.* **2021**, *60* (12), 6518–6525. https://doi.org/10.1002/anie.202014677.

(60) Cameron, J. M.; Fujimoto, S.; Wei, R.-J.; Newton, G. N.; Oshio, H. Post-Functionalization of a Photoactive Hybrid Polyoxotungstate. *Dalton Trans.* **2018**, *47* (31), 10590–10594. https://doi.org/10.1039/C8DT01253A.

(61) Li, C.; Suzuki, K.; Mizuno, N.; Yamaguchi, K. Polyoxometalate LUMO Engineering: A Strategy for Visible-Light-Responsive Aerobic Oxygenation Photocatalysts. *Chem. Commun.* **2018**, *54* (52), 7127–7130. https://doi.org/10.1039/C8CC03519A.

(62) Anjass, M.; Lowe, G. A.; Streb, C. Molecular Vanadium Oxides for Energy Conversion and Energy Storage: Current Trends and Emerging Opportunities. *Angew. Chem. Int. Ed.* **2021**, *60* (14), 7522–7532. https://doi.org/10.1002/anie.202010577.

(63) Bencini, A.; Bertini, I.; Gatteschi, D.; Scozzafava, A. Single-Crystal ESR Spectra of Copper(II) Complexes with Geometries Intermediate between a Square Pyramid and a Trigonal Bipyramid. *Inorg. Chem.* **1978**, *17* (11), 3194–3197. https://doi.org/10.1021/ic50189a047.

(64) Garribba, E.; Micera, G. The Determination of the Geometry of Cu(II) Complexes: An EPR Spectroscopy Experiment. *J. Chem. Educ.* **2006**, *83* (8), 1229. https://doi.org/10.1021/ed083p1229.

(65) Harmalker, S. P.; Pope, M. T. Hopping and Delocalized Electrons in Class II Mixed-Valence Oxovanadates. *J. Am. Chem. Soc.* **1981**, *103* (24), 7381–7383. https://doi.org/10.1021/ja00414a079.

(66) Zhang, T.; Solé-Daura, A.; Hostachy, S.; Blanchard, S.; Paris, C.; Li, Y.; Carbó, J. J.; Poblet, J. M.; Proust, A.; Guillemot, G. Modeling the Oxygen Vacancy at a Molecular Vanadium(III) Silica-Supported Catalyst. *J. Am. Chem. Soc.* **2018**, *140* (44), 14903–14914. https://doi.org/10.1021/jacs.8b09048.

(67) Rinfray, C.; Renaudineau, S.; Izzet, G.; Proust, A. A Covalent Polyoxomolybdate-Based Hybrid with Remarkable Electron Reservoir Properties. *Chem. Commun.* **2014**, *50* (62), 8575–8577. https://doi.org/10.1039/C4CC03779K.
(68) Sasaki, Y.; Yamase, T.; Ohashi, Y.; Sasada, Y. Structural Retention of Decatungstates upon Photoreduction. *Bull. Chem. Soc. Jpn.* **1987**, *60* (12), 4285–4290. https://doi.org/10.1246/bcsj.60.4285.
(69) Jacquet, J.; Blanchard, S.; Derat, E.; Murr, M. D.-E.; Fensterbank, L. Redox-Ligand Sustains Controlled Generation of CF3 Radicals by Well-Defined Copper Complex. *Chem. Sci.* **2016**, *7*, 2030–2036. https://doi.org/10.1039/C5SC03636D.
(70) Stoll, S.; Schweiger, A. EasySpin, a Comprehensive Software Package for Spectral Simulation and Analysis in EPR. *J. Magn. Reson.* **2006**, *178* (1), 42–55. https://doi.org/10.1016/j.jmr.2005.08.013.
(71) Dolomanov, O. V.; Bourhis, L. J.; Gildea, R. J.; Howard, J. a. K.; Puschmann, H. OLEX2: A Complete Structure Solution, Refinement and Analysis Program. *J. Appl. Crystallogr.* **2009**, *42* (2), 339–341. https://doi.org/10.1107/S0021889808042726.
(72) Sheldrick, G. M. SHELXT – Integrated Space-Group and Crystal-Structure Determination. *Acta Crystallogr. Sect. Found. Adv.* **2015**, *71* (1), 3–8. https://doi.org/10.1107/S2053273314026370.
(73) Sheldrick, G. M. Crystal Structure Refinement with SHELXL. *Acta Crystallogr. Sect. C Struct. Chem.* **2015**, *71* (1), 3–8. https://doi.org/10.1107/S2053229614024218.
(74) Neese, F. The ORCA Program System. *WIREs Comput. Mol. Sci.* **2012**, *2* (1), 73–78. https://doi.org/10.1002/wcms.81.
(75) Perdew, J. P. Erratum: Density-Functional Approximation for the Correlation Energy of the Inhomogeneous Electron Gas. *Phys Rev B* **1986**, *34* (10), 7406–7406. https://doi.org/10.1103/PhysRevB.34.7406.
(76) Becke, A. D. Density-Functional Exchange-Energy Approximation with Correct Asymptotic Behavior. *Phys Rev A* **1988**, *38* (6), 3098–3100. https://doi.org/10.1103/PhysRevA.38.3098.
(77) Neese, F. An Improvement of the Resolution of the Identity Approximation for the Formation of the Coulomb Matrix. *J. Comput. Chem.* **2003**, *24* (14), 1740–1747. https://doi.org/10.1002/jcc.10318.
(78) Weigend, F. Accurate Coulomb-Fitting Basis Sets for H to Rn. *Phys. Chem. Chem. Phys.* **2006**, *8* (9), 1057–1065. https://doi.org/10.1039/B515623H.
(79) Schäfer, A.; Huber, C.; Ahlrichs, R. Fully Optimized Contracted Gaussian Basis Sets of Triple Zeta Valence Quality for Atoms Li to Kr. *J. Chem. Phys.* **1994**, *100* (8), 5829–5835. https://doi.org/10.1063/1.467146.
(80) Weigend, F.; Ahlrichs, R. Balanced Basis Sets of Split Valence, Triple Zeta Valence and Quadruple Zeta Valence Quality for H to Rn: Design and Assessment of Accuracy. *Phys. Chem. Chem. Phys.* **2005**, *7* (18), 3297–3305. https://doi.org/10.1039/B508541A.
(81) Grimme, S.; Antony, J.; Ehrlich, S.; Krieg, H. A Consistent and Accurate *Ab Initio* Parametrization of Density Functional Dispersion Correction (DFT-D) for the 94 Elements H-Pu. *J. Chem. Phys.* **2010**, *132* (15), 154104. https://doi.org/10.1063/1.3382344.
(82) Grimme, S.; Ehrlich, S.; Goerigk, L. Effect of the Damping Function in Dispersion Corrected Density Functional Theory. *J. Comput. Chem.* **2011**, *32* (7), 1456–1465.
(83) Becke, A. D. A New Mixing of Hartree–Fock and Local Density-functional Theories. *J. Chem. Phys.* **1993**, *98* (2), 1372–1377. https://doi.org/10.1063/1.464304.
(84) Lee, C.; Yang, W.; Parr, R. G. Development of the Colle-Salvetti Correlation-Energy Formula into a Functional of the Electron Density. *Phys. Rev. B* **1988**, *37* (2), 785–789. https://doi.org/10.1103/PhysRevB.37.785.
(85) Noodleman, L. Valence Bond Description of Antiferromagnetic Coupling in Transition Metal Dimers. *J. Chem. Phys.* **1981**, *74* (10), 5737–5743. https://doi.org/10.1063/1.440939.
(86) Noodleman, L.; Case, D. A. Density-Functional Theory of Spin Polarization and Spin Coupling in Iron—Sulfur Clusters. In *Advances in Inorganic Chemistry*; Cammack, R., Ed.; Academic Press, 1992; Vol. 38, pp 423–470. https://doi.org/10.1016/S0898-8838(08)60070-7.
(87) Noodleman, L.; Davidson, E. R. Ligand Spin Polarization and Antiferromagnetic Coupling in Transition Metal Dimers. *Chem. Phys.* **1986**, *109* (1), 131–143. https://doi.org/10.1016/0301-0104(86)80192-6.

(88) Barone, V.; Cossi, M. Quantum Calculation of Molecular Energies and Energy Gradients in Solution by a Conductor Solvent Model. *J. Phys. Chem. A* **1998**, *102* (11), 1995–2001. https://doi.org/10.1021/jp9716997.
(89) Perdew, J. P.; Ernzerhof, M.; Burke, K. Rationale for Mixing Exact Exchange with Density Functional Approximations. *J. Chem. Phys.* **1996**, *105* (22), 9982–9985. https://doi.org/10.1063/1.472933.
(90) Gómez-Piñeiro, R. J.; Pantazis, D. A.; Orio, M. Comparison of Density Functional and Correlated Wave Function Methods for the Prediction of Cu(II) Hyperfine Coupling Constants. *ChemPhysChem* **2020**, *21* (24), 2667–2679.
(91) Lenthe, E. van; Baerends, E. J.; Snijders, J. G. Relativistic Regular Two-component Hamiltonians. *J. Chem. Phys.* **1993**, *99* (6), 4597–4610. https://doi.org/10.1063/1.466059.
(92) van Lenthe, E.; Baerends, E. J.; Snijders, J. G. Relativistic Total Energy Using Regular Approximations. *J. Chem. Phys.* **1994**, *101* (11), 9783–9792. https://doi.org/10.1063/1.467943.
(93) Pantazis, D. A.; Chen, X.-Y.; Landis, C. R.; Neese, F. All-Electron Scalar Relativistic Basis Sets for Third-Row Transition Metal Atoms. *J. Chem. Theory Comput.* **2008**, *4* (6), 908–919. https://doi.org/10.1021/ct800047t.
(94) Pantazis, D. A.; Neese, F. All-Electron Scalar Relativistic Basis Sets for the Lanthanides. *J. Chem. Theory Comput.* **2009**, *5* (9), 2229–2238. https://doi.org/10.1021/ct900090f.